CCFE
CULHAM CENTRE FOR FUSION ENERGY

UK Atomic Energy Authority

UKAEA-CCFE-PR(19)30

H. J. C. Oliver, S. E. Sharapov, B. N. Breizman, A. K. Fontanilla, D. A. Spong, D. Terranova and JET Contributors

Modification of the Alfven wave spectrum by pellet injection

Modification of the Alfven wave spectrum by pellet injection

H. J. C. Oliver, S. E. Sharapov, B. N. Breizman, A. K. Fontanilla, D. A. Spong, D. Terranova and JET Contributors

This is a preprint of a paper submitted for publication in Nuclear Fusion

Modification of the Alfvén wave spectrum by pellet injection

H. J. C. Oliver[1,2], S. E. Sharapov[2], B. N. Breizman[1], A. K. Fontanilla[1], D. A. Spong[3], D. Terranova[4], and JET Contributors ‡.

EUROfusion Consortium, JET, Culham Science Centre, Abingdon OX14 3DB, United Kingdom of Great Britain and Northern Ireland
[1] Institute for Fusion Studies, The University of Texas, Austin, TX 78712, USA
[2] UKAEA-CCFE, Culham Science Centre, Abingdon, Oxon, OX14 3DB, UK
[3] Oak Ridge National Laboratory, Oak Ridge, Tennessee, 37831-6169, USA
[4] Consorzio RFX, I-35127 Padova, Italy

E-mail: `hjcoliver@utexas.edu`

Abstract.

Alfvén eigenmodes driven by energetic particles are routinely observed in tokamak plasmas. These modes consist of poloidal harmonics of shear Alfvén waves coupled by inhomogeneity in the magnetic field. Further coupling is introduced by 3D inhomogeneities in the ion density during the assimilation of injected pellets. This additional coupling modifies the Alfvén continuum and discrete eigenmode spectrum. The frequencies of Alfvén eigenmodes drop dramatically when a pellet is injected in JET. From these observations, information about the changes in the ion density caused by a pellet can be inferred. To use Alfvén eigenmodes for MHD spectroscopy of pellet injected plasmas, the 3D MHD codes Stellgap and AE3D were generalised to incorporate 3D density profiles. A model for the expansion of the ionised pellet plasmoid along a magnetic field line was derived from the fluid equations. Thereby, the time evolution of the Alfvén eigenfrequency is reproduced. By comparing the numerical frequency drop of a toroidal Alfvén eigenmode (TAE) to experimental observations, the initial ion density of a cigar-shaped ablation region of length 4cm is estimated to be $n_* = 6.8 \times 10^{22}$ m^{-3} at the TAE location ($r/a \approx 0.75$). The frequency sweeping of an Alfvén eigenmode ends when the ion density homogenises poloidally. Modelling suggests that the time for poloidal homogenisation of the ion density at the TAE position is $\tau_h = 18 \pm 4$ ms for inboard pellet injection, and $\tau_h = 26 \pm 2$ ms for outboard pellet injection. By reproducing the frequency evolution of the elliptical Alfvén eigenmode (EAE), the initial ion density at the EAE location ($r/a \approx 0.9$) can be estimated to be $n_* = 4.8 \times 10^{22}$ m^{-3}. Poloidal homogenisation of the ion density takes 2.7 times longer at the EAE location than at the TAE location for both inboard and outboard pellet injection.

MHD spectroscopy, Alfvén eigenmodes, pellet injection

‡ See the author list of "Overview of the JET preparation for Deuterium-Tritium Operation" by E. Joffrin et al. to be published in Nuclear Fusion Special issue: overview and summary reports from the 27th Fusion Energy Conference (Ahmedabad, India, 22-27 October 2018).

1. Introduction

Alfvén eigenmodes (AEs) driven unstable by energetic particles are ubiquitous in tokamaks with axisymmetric magnetic fields, and stellerators with 3D magnetic fields[1]. The most frequently observed Alfvén eigenmodes are weakly damped modes with eigenfrequencies that lie inside gaps in the Alfvén continuum. These continuum gaps, and the gap modes within them, are created when poloidal harmonics of the shear Alfvén wave are coupled by poloidal modulation in the magnetic field. For example, the magnetic field is poloidally asymmetric in toroidal magnetic confinement devices. Therefore toroidicity couples neighbouring poloidal harmonics (denoted by the poloidal mode numbers m and $m-1$), creating the toroidal Alfvén eigenmode [2] (TAE). In plasmas with elliptical cross-sections, ellipticity of the magnetic surfaces introduces further poloidal asymmetry. Ellipticity couples the m and $m-2$ poloidal harmonics, producing the elliptical Alfvén eigenmode (EAE) [3, 4]. Poloidal and toroidal symmetries are broken in 3D magnetic configurations by poloidal and toroidal modulation of the magnetic field. As a result, toroidal harmonics are also coupled, producing helicity-induced gaps and helical Alfvén eigenmodes [5] (HAEs).

The possible coupling of Alfvén eigenmode harmonics introduced by 3D inhomogeneities in the plasma mass density is examined in this paper. Such 3D density inhomogeneities are transiently caused by the injection of frozen pellets, which are used to refuel the core of the plasma, control edge localised modes (ELMs), and mitigate disruptions [6, 7, 8]. These varied applications require pellets with drastically different parameters, for example, pellet size, material, trajectory, velocity, and injection frequency are all tailored to fit the application. As a result, the timescales of pellet assimilation can vary dramatically depending on the experiment and machine.

Diagnosing the effect of the pellet on the plasma represents an important but challenging task, because of the short life-time of the pellet and the complexity of the pellet assimilation into the plasma. We investigate whether key pellet parameters can be assessed using magnetohydrodynamic (MHD) spectroscopy [9] based on Alfvén eigenmodes observed during pellet injection [10]. MHD spectroscopy — the diagnosis of plasma properties through observations of MHD spectrum of waves and instabilities — is currently used to diagnose the time evolution of the safety factor profile in tokamaks [11, 12]. MHD spectroscopy based on Alfvén eigenmodes offers excellent time resolution, and provides information on the density of ions in the core, rather than the density of neutral atoms delivered by the pellet. For this reason, we apply MHD spectroscopy to pellet injected plasmas for the first time. MHD spectroscopy can complement other diagnostics that are commonly used to study the plasma density, such as interferometry, LIDAR and Thompson scattering, which measure the electron density, and D_α spectroscopy measuring the density of deuterium atoms.

The ions deposited by the injected pellet introduce poloidal and toroidal dependence in the ion density, which causes the Alfvén velocity to be periodic in poloidal and toroidal angle. Therefore, the refractive index is periodic, coupling the poloidal and toroidal harmonics of the Alfvén wave. This coupling significantly modifies the Alfvén continuum and discrete eigenmode spectrum. Information about the changes in the ion density caused by pellets can be inferred from observed changes in the frequency of Alfvén eigenmodes.

To better understand the relationship between the eigenfrequency and the 3D ion density profiles, we modified the 3D MHD codes Stellgap [13] and AE3D [14], which are routinely used to study Alfvén eigenmodes in stellerators. Stellgap and AE3D were generalised to incorporate 3D ion density profiles, in addition to the 3D magnetic field. A model that describes the 1D expansion of pellet material along magnetic field lines is derived from the fluid equations. The 3D ion density profiles resulting from pellet injection are obtained by mapping this 1D expansion onto the magnetic field lines. From these 3D density profiles, we use the modified AE3D to calculate the Alfvén eigenmodes for pellet injected plasmas.

First, the experimental motivation for this study is presented in Section 2. Next, analytical estimates for the Alfvén continuum and TAEs for a tokamak plasma with poloidal modulation of the ion mass density are derived in Section 3 and compared to numerical results in Sections 4. A model for the expansion of the pellet material is introduced in Section 5 to study the effect of pellets on Alfvén eigenmodes in JET plasmas in Section 6. Finally, these results are discussed in Section 7 and summarised in Section 8.

2. Experimental observations

In this article, we examine plasmas produced in the Joint European Torus (JET) [15] that are injected with frozen deuterium (D) pellets using the centrifugal pellet injector [16, 8]. The plasmas in this experiment had on-axis safety factor, $q_0 \lesssim 1$; major radius, $R_0 = 3.0$ m; minor radius, $a = 1.0$ m; on-axis equilibrium magnetic field, $B_0 = B(R_0) = 3.25$ T; and plasma current, $I_p \leq 2.5$ MA.

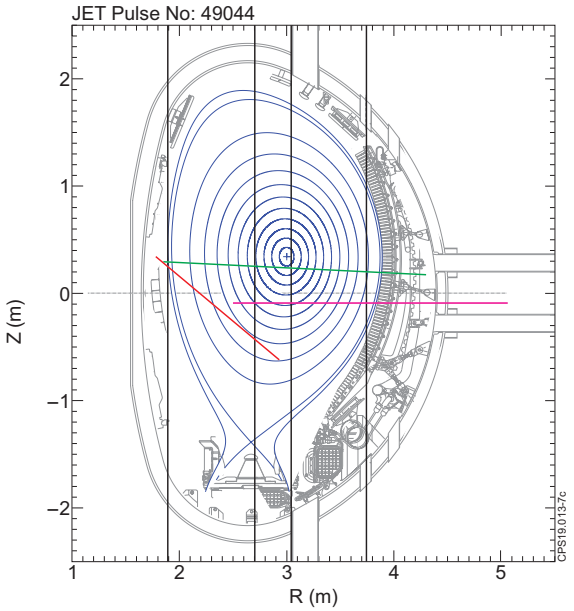

Figure 1: The poloidal cross-section of JET, showing the magnetic flux surfaces (blue), vertical lines of sight of the far infrared interferometer (black), LIDAR line of sight (green), inboard pellet injection track (red) and outboard pellet injection track (magenta) for shot #49044 at time $t = 17.89$ s.

The pellet injector cuts and accelerates 4mm cubic pellets, before injecting them into the plasma from either the inboard or outboard track, as illustrated in Figure 1. The fuelling pellets under consideration were injected at speeds $v_{pell} \sim 160$ ms^{-1} and deposit up to 3.8×10^{21} D atoms deep in the plasma. This injection of particles can approximately double the plasma density for JET plasmas with electron densities $n_e \approx 1 - 5 \times 10^{19}$ m^{-3} and plasma volume ~ 100 m^3. Neither of the injection tracks crossed the magnetic axis, as shown in Figure 2, and so hollow electron density profiles are frequently observed after pellet injection. The inboard trajectory is tangential to the flux surface at $r/a \approx 0.6$. Most of the pellet material is deposited in the first 1.15m of the inboard trajectory, leading up to the tangent point [16].

The electron density radial profile, $n_e(r)$, was

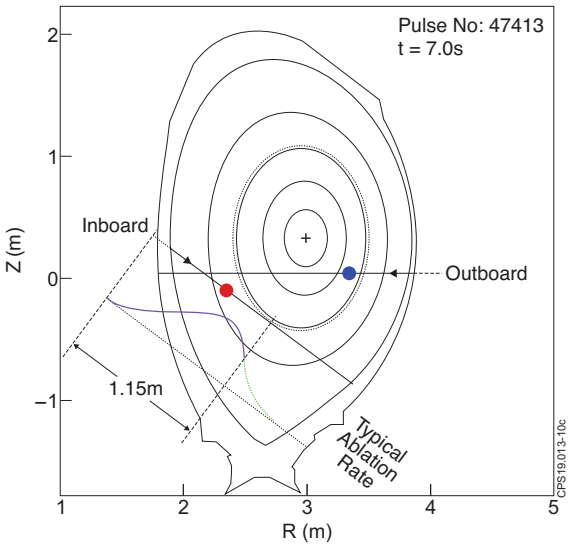

Figure 2: Geometry of the inboard and outboard pellet injection trajectories in a typical JET equilibrium [16]. The typical ablation profile for a pellet injected from the inboard side is shown.

measured using LIDAR [17], along the line of sight shown in Figure 1, at time intervals of 250 ms. This low time resolution was insufficient to consistently measure the electron density profile on timescales comparable to the characteristic timescales of pellet ablation and homogenisation. Highly poloidally asymmetric electron density profiles were observed despite this limitation. Figure 3 shows an electron density profile that was still highly asymmetric 22 ms after pellet injection from the inboard side. Similar poloidally asymmetric electron density profiles were observed up to 43 ms after pellet injection.

Interferometry provides better time resolution than the LIDAR diagnostic, as demonstrated in Figure 4. However, the radial resolution of interferometry is limited, with only four lines of sight. Two of these lie at the plasma edge, and two lie close to the magnetic axis, as shown in Figure 1. None of the lines of sight intersect where most of the pellet material is deposited.

During this experiment, TAEs and EAEs were excited by fast ions produced by ion cyclotron resonance heating (ICRH) heating with high powers of $P_{ICRH} = 4 - 8$MW, as shown for discharge #49044 in Figure 4. The Alfvén eigenmodes studied here were excited by radial gradients of trapped energetic hydrogen minority ions with concentrations $n_H/n_e \sim 2 - 5\%$.

Alfvén eigenmodes were detected using toroidally separated Mirnov coils positioned outside the plasma surface [18]. These magnetic coils measure the time-varying perturbed poloidal magnetic field produced

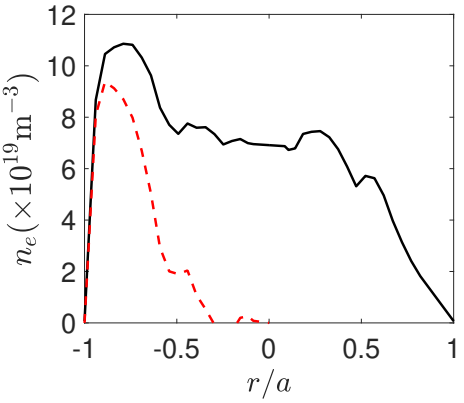

Figure 3: The electron density n_e (black solid) as a function of radius (r) normalised to minor radius (a), as measured by LIDAR at time $t = 19.63$ s in discharge #49032. Positive and negative radii correspond to the outboard and inboard side, respectively. The difference between the high field side and low field side is shown in dashed red.

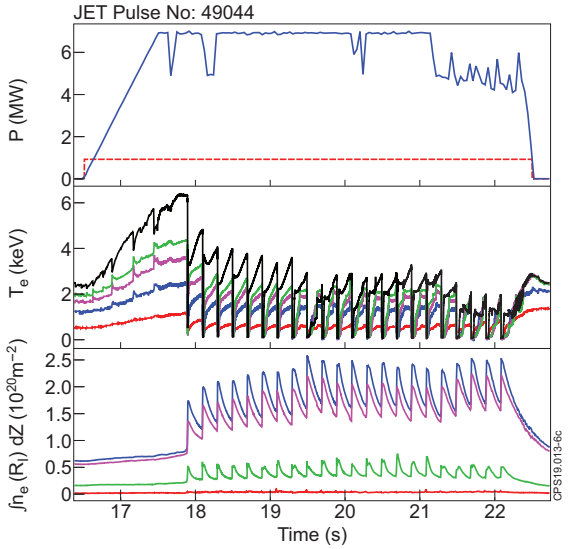

Figure 4: Heating waveforms and plasma parameters for JET discharge #49044. Top: ICRH (blue solid) and NBI (red dashed) heating power, P. Middle: Electron temperature T_e as measured by ECE radiometry at $R = 3.06, 3.29, 3.40, 3.54$, and 3.78 m (from top to bottom). Bottom: Line integrated electron density $\int n_e(R_I)\mathrm{dZ}$ as measured by far infrared interferometry along the line of sights at radii R_I, shown in Figure 1.

by the eigenmodes, $d(\delta B_\theta)/dt \sim \omega \delta B_\theta$. Toroidal mode numbers were calculated using the relative phase shifts of the magnetic perturbations at the different coil toroidal positions. With sampling rates of 1 MHz — in contrast to a sampling rate of 4 Hz for the LIDAR diagnostic — magnetic coils facilitate MHD spectroscopy with much higher time resolution than many conventional diagnostics.

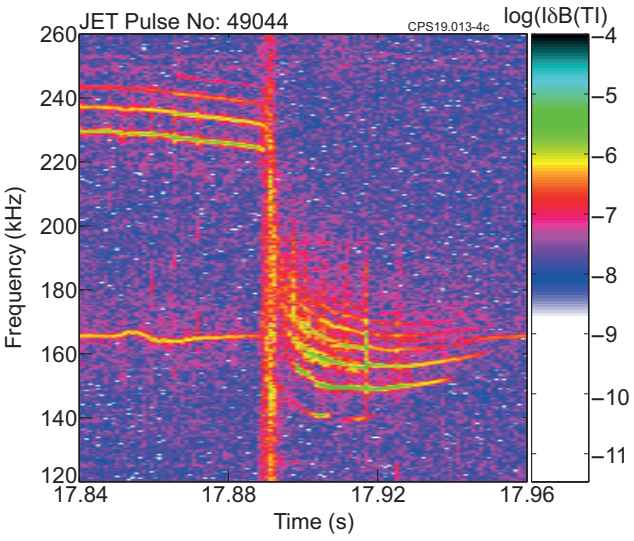

(a)

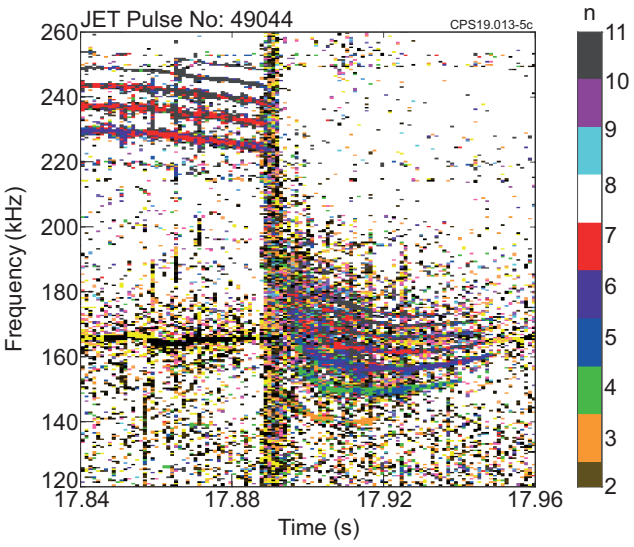

(b)

Figure 5: (a) Magnetic spectrograph showing the amplitude of the magnetic perturbation caused by a TAE before and after pellet injection in discharge #49044; (b) a phase magnetic spectrograph showing the toroidal mode numbers of the same TAE. The pellet was injected on the inboard track at time $t = 17.89$ s.

When pellets were injected into plasmas in which TAEs were already excited, the frequency of the TAE dropped, as shown in Figure 5. There was a period $\sim 3 - 8$ ms after pellet injection where the toroidal mode numbers of the TAE could not be determined, as shown in Figure 5b. There was a longer period

after pellet injection where toroidal mode numbers could be determined and dramatic changes in the TAE eigenfrequency were observed. There was a rapid drop in the TAE eigenfrequency in all discharges. This sweeping of the frequency occurs over $\sim 25 - 45$ ms.

The drop in frequency is larger for inboard injection versus outboard injection, as illustrated in Figures 5 and 6. Additionally, the spectrum of excited toroidal mode numbers often broadens, as shown in Figure 5b. New toroidal mode numbers are excited after pellet injection. These new toroidal harmonics persist as long as existing toroidal harmonics.

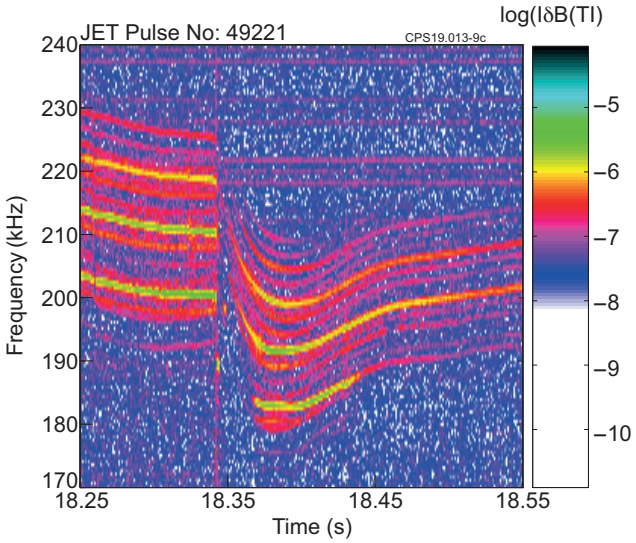

Figure 6: Magnetic spectrograph showing the amplitude of the magnetic perturbation caused by a TAE before and after pellet injection in discharge #49221. The pellet was injected on the outboard track at time $t = 18.342$ s.

The frequencies of elliptical Alfvén eigenmodes (EAEs) also drop dramatically after the injection and assimilation of the pellet material [10]. Occasionally, a delay in the drop in frequency is observed, as shown in Figure 7. The EAE frequencies continue to increase during this period. After a delay of $\sim 8 - 18$ ms, the frequency drops. The frequency sweeping of EAEs takes longer to stabilise than the frequency sweeping of TAEs. The period of frequency sweeping for EAEs continues for $\sim 55 - 115$ ms.

The differences in the timescale and magnitude of frequency sweeping between TAEs and EAEs, and between inboard (HFS) and outboard (LFS) pellet injection are summarised in Table 1.

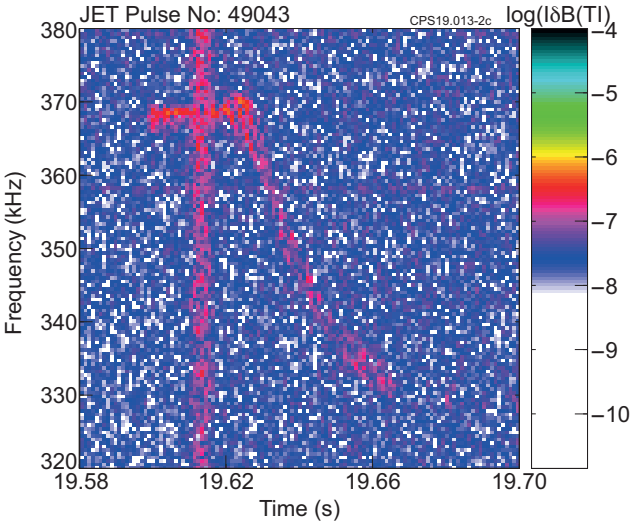

Figure 7: Magnetic spectrograph showing the amplitude of the magnetic perturbation due to an EAE before and after inboard pellet injection in discharge #49043 at time $t = 19.615$ s.

Parameter		TAE	EAE
$t_2 - t_1$ [ms]	HFS	30 ± 7	68 ± 10
	LFS	42 ± 5	93 ± 14
τ [ms]	HFS	18 ± 4	48 ± 12
	LFS	26 ± 2	69 ± 12
$\frac{\Delta f}{f_1}$	HFS	0.29 ± 0.06	0.11 ± 0.05
	LFS	0.10 ± 0.01	0.10 ± 0.02

Table 1: A comparison of the timescales and fractional changes in frequency for frequency sweeping of TAEs and EAEs in plasmas where a pellet is injected from the inboard (HFS) or outboard (LFS). t_2 and t_1 are the time at the beginning and bottom of frequency sweeping, $f_1 = f(t_1)$ is the initial frequency, and $\Delta f = f(t_1) - f(t_2)$ is the frequency decrease. The characteristic sweeping period τ is defined as $f(\tau) = 1.01 f(t_2)$. The mean value and standard deviation are calculated for each variable.

3. Analytical estimates of the Alfvén spectrum in toroidal plasmas with poloidal modulation of the ion density

We begin the analysis of the observations in Section 2 by deriving analytical estimates for the TAE radial structure and eigenfrequency. These provide a benchmark for the numerical work, and aid our understanding of the effect of ion density asymmetries on TAEs. We solve the high mode number shear Alfvén wave equation [19, 20]:

$$\mathbf{B_0}\cdot\nabla\left(\frac{1}{B_0}\nabla_\perp^2\left(\frac{\mathbf{B_0}}{B_0}\cdot\nabla\phi\right)\right)+\nabla\cdot\left(\frac{\omega^2}{v_A^2}\nabla_\perp\phi\right)=0. \quad (1)$$

The wave electrostatic potential ϕ for TAE with toroidal mode number n is represented as a Fourier series:

$$\phi(\mathbf{r}) = \mathrm{e}^{\mathrm{i}(n\zeta-\omega t)}\sum_m \phi_m(r)\mathrm{e}^{-\mathrm{i}m\theta} + c.c.. \quad (2)$$

where m and n are the poloidal and toroidal mode numbers, and θ and ζ are the poloidal and toroidal angles. We can write the electrostatic potential as a Fourier series due to the periodicity of the eigenmode in poloidal and toroidal angle. The radial structure of a given poloidal harmonic, $\phi_m(r)$, is localised in radius.

Working in flux coordinates (r,θ,ζ), the shear Alfvén wave equation can be rewritten using the contravariant metric tensor for a low β, large aspect ratio ($a/R_0 \ll 1$) tokamak with circular cross-section:

$$\mathcal{J}g^{rr} \approx rR_0\left(1+2\left(\frac{r}{R_0}+\Delta'\right)\cos\theta\right), \quad (3)$$

$$\mathcal{J}g^{r\theta} \approx -R_0\left(\frac{r}{R_0}+(r\Delta')'\right)\sin\theta \quad (4)$$

$$\mathcal{J}g^{\theta\theta} \approx \frac{R_0}{r}\left(1-2\Delta'\cos\theta\right), \quad (5)$$

where primes denote derivatives with respect to the flux coordinate r and the Jacobian is:

$$\mathcal{J} \approx rR_0\left(1-2\frac{r}{R_0}\cos\theta\right). \quad (6)$$

The ion mass density ϱ_i is no longer simply a function of the flux coordinate r. For ease, the poloidal inhomogeneity in ion density is assumed to be a modulation:

$$\varrho_i(r,\theta) = \varrho_{i0}(r)\left[1+\delta\cos\theta\right], \quad (7)$$

where δ is the size of poloidal modulation and ϱ_{i0} is the ion mass density at $(r,\theta,\zeta)=(r,0,0)$. For an inhomogeneity peaking on the high field side, $\delta<0$, for an inhomogeneity peaking on the low field side, $\delta>0$.

The two poloidal harmonics ϕ_m and ϕ_{m-1} are decoupled in a cylindrical plasma with circular cross-section and poloidally homogeneous ion density. Therefore, the two second-order eigenmode equations are singular at $\omega_1^2 = k_{\parallel_m}^2 v_A^2$ and $\omega_2^2 = k_{\parallel_{m-1}}^2 v_A^2$, respectively. The poloidal inhomogeneity due to toroidicity and ion density couples the m and $m-1$ poloidal harmonics, and the two eigenmode equations.

The two coupled eigenmode equations can be simplified by only considering frequencies close to $\omega_1^2 = k_{\parallel_m}^2 v_A^2$ and $\omega_2^2 = k_{\parallel_{m-1}}^2 v_A^2$, respectively. If magnetic shear $S = r/q\cdot\mathrm{dq/dr}$ is small, we obtain two coupled equations for the m and $m-1$ poloidal harmonics:

$$\mathcal{L}_m\phi_m + \frac{(2\varepsilon+\delta)}{8q^2R_0^2}\frac{\mathrm{d}^2\phi_{\mathrm{m-1}}}{\mathrm{d}r^2} = 0, \quad (8)$$

$$\mathcal{L}_{m-1}\phi_{m-1} + \frac{(2\varepsilon+\delta)}{8q^2R_0^2}\frac{\mathrm{d}^2\phi_{\mathrm{m}}}{\mathrm{d}r^2} = 0, \quad (9)$$

where $\varepsilon = 5r_m/2R_0$ [21], and the operator $\mathcal{L}_m$ is given by:

$$\mathcal{L}_m = \frac{\mathrm{d}}{\mathrm{d}r}\left[\left(\frac{\omega^2}{v_A^2}-k_{\parallel_m}^2\right)\frac{\mathrm{d}}{\mathrm{d}r}\right] - \frac{m^2}{r^2}\left(\frac{\omega^2}{v_A^2}-k_{\parallel_m}^2\right) \quad (10)$$

Equations 8 and 9 describe two coupled "cylindrical" modes in the vicinity of the rational flux surface that satisfies the condition:

$$q(r_m) = \frac{m-1/2}{n}. \quad (11)$$

The Alfvén continuum is obtained when the determinant of the coefficients of the second order terms in the coupled eigenmode equations equals zero [22]. This yields the normalised size of gaps in the continuum induced by toroidicity and the poloidal modulation of ion density is given by:

$$\frac{\omega_+^2-\omega_-^2}{\omega_+^2+\omega_-^2} = \varepsilon+\frac{\delta}{2} \quad (12)$$

where ω_+ and ω_- are the frequencies at the top and bottom of the continuum gap. The width of the gap is normalised to the frequency at the centre of the gap, $\omega_0 = v_A/2qR_0$.

The two poloidal harmonics are strongly coupled at $r=r_m$. The region in the vicinity of the gap surface is referred to as the inner region. Equations 8 and 9 can be solved in the inner region by following a similar method to that of Breizman and Sharapov [23, 24]. First, the equations are normalised by introducing the dimensionless frequency,

$$g = \frac{2}{2\varepsilon+\delta}\left(\frac{4q^2R_0^2\omega^2}{v_A^2}-1\right), \quad (13)$$

and the dimensionless radial variable,

$$x = nq(r)-m+\frac{1}{2} \approx mS\frac{r-r_m}{r_m}. \quad (14)$$

In the inner layer, derivatives of the potential dominate over derivatives of equilibrium variables (denoted by F), and non-derivative terms, $\mathrm{d}\phi/\mathrm{dr} \gg \mathrm{m}\phi/\mathrm{r}, \mathrm{dF/dr}$. By Taylor expanding $\omega^2/v_A^2 - k_{\parallel_m}^2$ and

$\omega^2/v_A^2 - k^2_{\parallel_{m-1}}$ about $x = 0$, the eigenmode equations can be written:

$$\frac{\mathrm{d}}{\mathrm{d}z}\left[(g+z)\,\frac{\mathrm{d}\phi_{\mathrm{m}}}{\mathrm{d}z}\right] + \frac{\mathrm{d}^2\phi_{\mathrm{m-1}}}{\mathrm{d}z^2} \simeq 0, \tag{15}$$

$$\frac{\mathrm{d}}{\mathrm{d}z}\left[(g-z)\,\frac{\mathrm{d}\phi_{\mathrm{m-1}}}{\mathrm{d}z}\right] + \frac{\mathrm{d}^2\phi_{\mathrm{m}}}{\mathrm{d}z^2} \simeq 0, \tag{16}$$

where $z = 8x/(2\varepsilon + \delta)$. Integrating once, and defining $U(z) = \mathrm{d}\phi_m/\mathrm{d}z$ and $V(z) = \mathrm{d}\phi_{m-1}/\mathrm{d}z$ yields:

$$\begin{aligned}(g+z)\,U + V &= C_m,\\ (g-z)\,V + U &= -C_{m-1},\end{aligned} \tag{17}$$

where C_m and C_{m-1} are constants of integration. The solution for the wave potential in the inner region is found by re-arranging for U and V, and integrating once more:

$$\begin{aligned}\phi_m^{in} = &-\frac{C_{m-1} + gC_m}{\sqrt{1-g^2}}\tan^{-1}\left(\frac{z}{\sqrt{1-g^2}}\right)\\ &+ \frac{C_m}{2}\ln\left|1-g^2+z^2\right| + const.,\end{aligned} \tag{18}$$

$$\begin{aligned}\phi_{m-1}^{in} = &+\frac{C_m + gC_{m-1}}{\sqrt{1-g^2}}\tan^{-1}\left(\frac{z}{\sqrt{1-g^2}}\right)\\ &+ \frac{C_{m-1}}{2}\ln\left|1-g^2+z^2\right| + const..\end{aligned} \tag{19}$$

The inner width of the mode is described by $z \sim \sqrt{1-g^2}$:

$$\Delta^{in} \simeq \left(\varepsilon + \frac{\delta}{2}\right)\frac{r_m}{m}\frac{\pi}{4}. \tag{20}$$

Coupling effects are not important in the outer region [24] so terms containing coupling parameters δ and ε can be neglected from Equations 8 and 9. Therefore, we look for solutions of $\mathcal{L}_m\phi_m = 0$. For low shear S,

$$\phi_m^{out} = C_m \exp\left(-\frac{|x|}{S}\right) U\left(\frac{1}{2} - \frac{S}{2}\frac{x}{|x|}, 1, \frac{2|x|}{S}\right), \tag{21}$$

$$\phi_{m-1}^{out} = C_{m-1} \exp\left(-\frac{|x|}{S}\right) U\left(\frac{1}{2} + \frac{S}{2}\frac{x}{|x|}, 1, \frac{2|x|}{S}\right), \tag{22}$$

where $U(a,b,y)$ is the confluent hypergeometric function [25]. The outer width of the mode $\Delta^{out} = r_m/m$ is also unaffected by the poloidal inhomogeneity in the plasma density.

The inner layer solutions (in the limit $z \to \pm\infty$) are asymptotically matched to the outer layer solutions (in the limit $x \to 0$). The TAE eigenfrequency is found by equating the jump of the inner solution to the jump of the outer solution for each of the two poloidal harmonics:

$$\phi^{in}|_{x=0^+} - \phi^{in}|_{x=0^-} = \phi^{out}|_{x=0^+} - \phi^{out}|_{x=0^-}. \tag{23}$$

The two jump conditions yield a dispersion relation, which has the solutions:

$$g = \pm 1, \pm\left(-1 + \frac{8}{4+\pi^2 S^2}\right). \tag{24}$$

These solutions correspond to the upper and lower continuum, and the odd and even TAE, respectively. Returning to dimensionalised variables, the solutions of the dispersion relation give the TAE eigenfrequencies:

$$\omega = \frac{v_A}{2qR_0}\left[1 \pm \frac{1}{2}\left(\varepsilon + \frac{\delta}{2}\right)\left(1 - \frac{\pi^2 S^2}{2}\right)\right], \tag{25}$$

where $\pm$ corresponds to the odd and even modes respectively. There are two distinct effects related to changes in density that change the TAE eigenfrequency. First, increasing the ion density causes the Alfvén velocity to decrease, and therefore the eigenfrequency to decrease. Second, a change in the inhomogeneity of the ion density changes the coupling of the poloidal harmonics in the TAE, causing the eigenfrequency to change. As the size of inhomogeneity peaked on the low field side ($\delta > 0$) increases, the frequency of an even TAE will decrease. Conversely, for an inhomogeneity peaking on the high field side ($\delta < 0$), the frequency of an even TAE will increase with the size of inhomogeneity.

4. Numerical study of the Alfvén spectrum in toroidal plasmas with poloidal modulation of the ion density

To elucidate the effect of 3D inhomogeneities in the ion mass density on the Alfvén spectrum, we first consider the simpler problem of modulation in the ion mass density. We begin by using a test equilibrium with circular poloidal cross-section, major radius $R_0 = 1$ m, minor radius $a = 0.3$ m, on-axis equilibrium magnetic field $B_0 = 1$ T. The aspect ratio is therefore similar to JET, but the equilibrium lacks the ellipticity and triangularity required to produce significant higher frequency gaps and modes.

4.1. Effect of poloidal modulation in ion density on the Alfvén continuum

3D ion density profiles are introduced to the ideal MHD code Stellgap [13], which is usually used

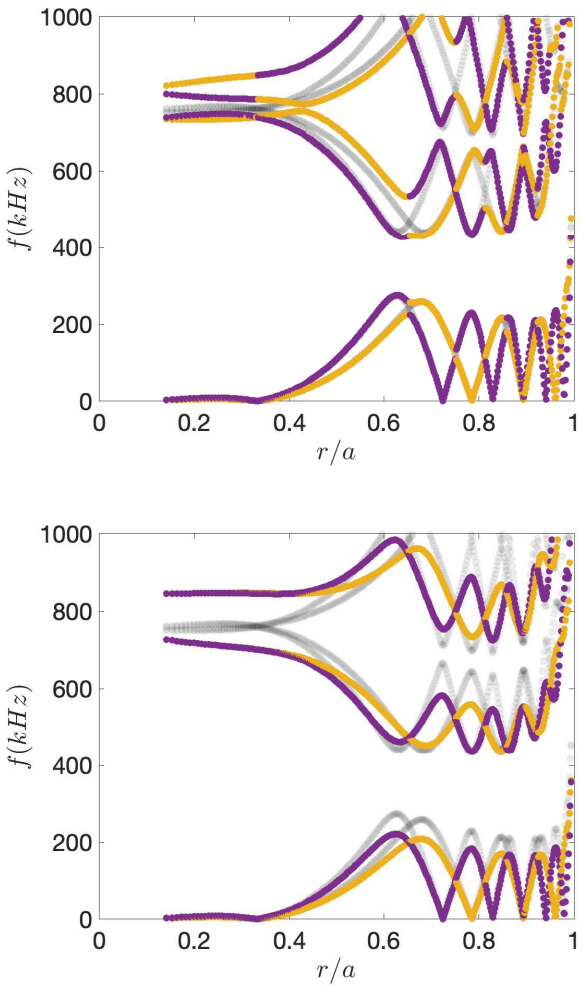

Figure 8: The Alfvén continua for the $n = 2$ (yellow) and $n = 3$ (purple) toroidal harmonics for a plasma with circular poloidal cross-section and (a) toroidal or (b) poloidal modulation of the ion mass density, with the size of inhomogeneity $\delta = 3/4$. The continuum for a plasma with homogeneous mass density is displayed in black.

to study the shear Alfvén continuum in the 3D magnetic configuration of stellarators. Introducing poloidal and toroidal modulation couples poloidal and toroidal harmonics, modifying the continuum. This is demonstrated in Figure 8a and 8b for modulation of the ion mass density:

$$\varrho_i = \varrho_{i0}\left(1 + \delta\cos\theta\right), \tag{26}$$

$$\varrho_i = \varrho_{i0}\left(1 + \delta\cos\zeta\right). \tag{27}$$

The toroidal modulation in the ion density produces new gaps where the continua of the two toroidal harmonics were degenerate in the toroidally symmetric case. The toroidal coupling does not significantly affect existing gaps, for example the toroidicity-induced gap of interest.

The poloidal modulation in ion mass density widens existing continuum gaps induced by poloidal inhomogeneity in the magnetic field caused by toroidicity. Higher frequency gaps also widen due to higher order coupling effects, $\mathcal{O}\left(\delta^i\right)$ for the ith gap. The size of the TAE continuum gap increases with the size of poloidal modulation of the ion density, as shown in Figure 9. The numerical result for the size of the TAE gap agrees well with the analytical estimate given by Equation 12.

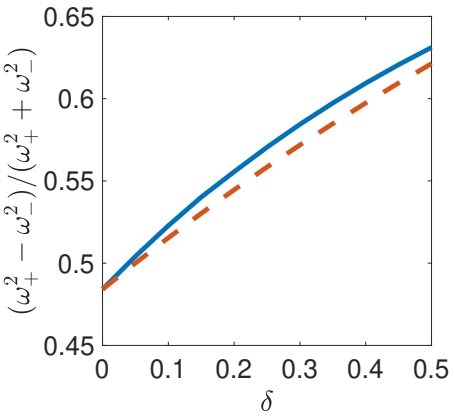

Figure 9: The size of the $n = 2$ TAE continuum gap increases with the size of poloidal modulation, δ. The frequency at the top and bottom of the TAE gap is denoted by ω_+ and ω_-, respectively. The numerical estimate (solid blue) agrees well with the analytical estimate (dashed orange).

4.2. Effect of poloidal modulation in ion density on Alfvén eigenfrequencies

To understand how poloidally asymmetric ion mass density profiles affect Alfvén eigenmodes, 3D density profiles are introduced to the MHD code AE3D [14]. AE3D is usually used to calculate the Alfvén eigenmodes present in 3D magnetic configurations of stellerators. With 3D ion density profiles incorporated, AE3D is now suitable for the study of Alfvén eigenmodes during pellet injection.

Four TAEs with toroidal mode number $n = 2$ are found within the continuum gap at frequencies 277 kHz, 312 kHz, 358 kHz, and 403 kHz for the circular equilibrium. All four TAEs are even TAEs — the two dominant poloidal harmonics ($m = 2$ and 3) have the same polarity. The modes differ due to the polarity of the $m = 4$ and 5 poloidal harmonics, with different permutations of the $\pm$ sign for the two harmonics.

Poloidal modulation of the ion mass density is introduced, $\varrho = \varrho_0 (1 + \delta \cos\theta)$. The eigenvalue of each TAE decreases as the size of poloidal inhomogeneity (δ) increases, as demonstrated in Figure 10. The decrease in eigenvalue with size of poloidal inhomogeneity found by AE3D closely matches that of the analytical estimate. The frequency of the gap centre does not decrease with δ, because the $\delta \cos\theta$ term averages to zero over the flux surface. The decrease in frequency shown in Figure 10 is entirely due to the increased coupling introduced by the poloidal inhomogeneity in mass density.

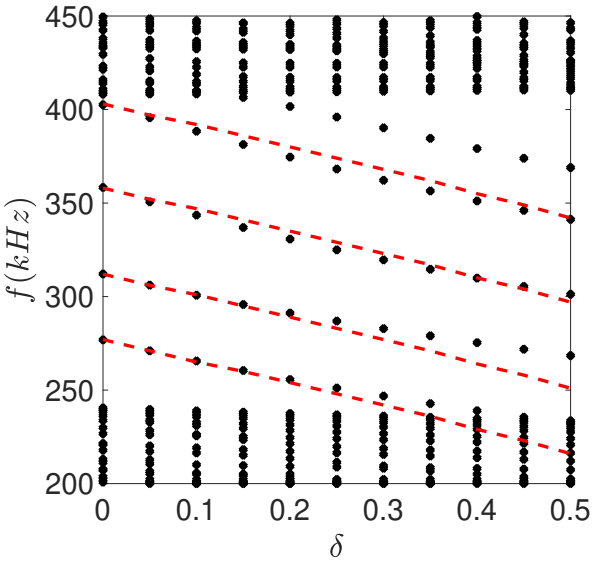

Figure 10: The eigenvalue (f) decreases with increasing size of poloidal modulation (δ) for poloidal modulation peaking on the low field side. The trend predicted analytically in Equation 25 (red dashed) agrees well with the results from AE3D (black dots). Modes at the top and bottom of the figure ($f > 410$ kHz and $f < 235$ kHz) are continuum modes.

5. Model for the expansion of the ionised pellet wake with heating by thermal electrons

With good agreement between the analytical estimates and numerical results for a simplified equilibrium and density profile, we move to a more realistic model. The axisymmetric equilibrium is reconstructed using the 3D equilibrium code VMEC [26] based on an EFIT [27] reconstruction for JET discharge #49044 at time $t = 17.62$ s. No constraints were available for the EFIT reconstruction, because the 1999 experiment predated the installation of the motional stark emission and Thomson scattering diagnostics. Constraint of the q profile reconstruction using MHD markers was not possible because neoclassical tearing modes and Alfvén cascades were not observed in the experiment.

The equilibrium density profile is considered to be static. The ion density profile due to the pellet material is calculated using a model for the expansion of a pellet wake heated by background electrons described below. This model is applied to produce a 3D density profile that is used as input for the code AE3D.

As a pellet moves through the plasma, it deposits a wake of neutral material that rapidly ionises. The cold, overdense plasmoid expands along the flux tube at approximately the wake ion sound speed c_s [28]. As the pellet expands, it is heated by thermal electrons.

5.1. Heating of the pellet wake by thermal electrons

Thermal electrons deposit energy in the wake due to collisional drag. The heating rate of the wake, Q, will vary along the wake depending on the local density. The energy deposited per unit volume per unit time by the background electrons due to drag is:

$$\begin{aligned} Q &= -\frac{\partial}{\partial t}\int \frac{1}{2} m_e n_b v^2 f \mathrm{d}^3 v \\ &= 4\pi m_e n_b \int v^4 \nu f \mathrm{d}v, \end{aligned} \tag{28}$$

where v is the thermal electron velocity, n_b is the density of the background electrons, m_e is the electron mass, f is the distribution function of the thermal electrons, $\nu = 8\pi(\varrho/m_i)e^4 \ln\Lambda / m_e^2 v^3$ is the collision frequency of thermal electrons with the wake [29], and ϱ is the ion mass density of the wake.

As the wake is heated, the background electrons cool down. Hence their distribution function is described by a slowing down distribution. Assuming the background is initially Maxwellian, the distribution function of the incident electrons is:

$$f(v,t) = \left(\frac{m_e}{2\pi T_b}\right)^{\frac{3}{2}} \exp\left[-\left(3\nu(\varrho, T_b)t + \frac{v^3}{v_b^3}\right)^{\frac{2}{3}}\right], \tag{29}$$

where $v_b = \sqrt{\gamma T_b / m_e}$ is the thermal velocity for background electrons at temperature T_b. The distribution function f is normalised such that: $n_b \int f \mathrm{d}^3 v = 1$.

5.2. Modelling the expansion of the pellet wake with the fluid equations

For the JET discharge under consideration, the background plasma temperature $T_b = 1$ keV, and the background plasma density $n_b = 10^{19}$ m^{-3}, and hence the equilibrium beta, $\beta_{eq} \approx 4 \times 10^{-4}$. Meanwhile, the

wake temperature $T \approx 10$ eV and wake density $n_w \approx 10^{23}$ m^{-3}, and so the wake beta, $\beta_w = 4 \times 10^{-2} \ll 1$. Additionally, the wake is a good electrical conductor because the skin depth is much smaller than the size of the wake, so the frozen-in condition applies to the wake. Therefore, the wake expansion perpendicular to the magnetic field lines is inhibited by the $\mathbf{j} \times \mathbf{B}$ force.

The 1D wake expansion along a magnetic field line is modelled using the fluid equations for an ideal gas. The continuity, momentum and energy equations are, respectively:

$$\frac{\partial \varrho}{\partial t} + \nabla \cdot (\varrho \mathbf{V}) = 0 \tag{30}$$

$$\frac{\partial}{\partial t}(\varrho \mathbf{V}) + \nabla \cdot (\varrho \mathbf{V}\mathbf{V}) + \nabla p = 0 \tag{31}$$

$$\frac{\partial}{\partial t}\left(\varrho\left[\frac{1}{2}V^2 + \epsilon\right]\right) + \nabla \cdot \left(\varrho \mathbf{V}\left[\frac{1}{2}V^2 + h\right]\right) = Q \tag{32}$$

where the following wake quantities are defined: mass of a wake ion, m_i; temperature, T; velocity, V; incident power density, Q; internal energy, $\epsilon = T/m_i(\gamma - 1)$; pressure, $p = \varrho T/m_i$; and enthalpy, $h = \epsilon + p/\varrho$.

By substituting the definitions for pressure, internal energy and enthalpy into Equations 31 and 32, we obtain:

$$\frac{\partial \mathbf{V}}{\partial t} + (\mathbf{V} \cdot \nabla)\mathbf{V} + \frac{1}{m_i}\nabla T + \frac{T}{m_i}\nabla \log \varrho = 0 \tag{33}$$

$$\frac{1}{\gamma - 1}\frac{\partial T}{\partial t} + T(\nabla \cdot \mathbf{V}) + \frac{1}{\gamma - 1}(\mathbf{V} \cdot \nabla)T = A \tag{34}$$

where $\gamma = 5/3$ is the adiabatic index, and $A = m_i Q/\varrho$ is the heating rate per wake particle. A is independent of the wake mass density, so the heating rate is constant along the wake. The wake variables are normalised using characteristic quantities for a cigar-shaped wake of length 4 cm:

$$\begin{aligned} t \to t\nu_*, L \to \frac{L}{V_*/\nu_*}, \varrho \to \frac{\varrho}{\varrho_*}, \\ V \to \frac{V}{V_*}, T \to \frac{T}{T_*}, A \to \frac{A}{\nu_* T_b} \end{aligned} \tag{35}$$

where L is the distance along the magnetic field line, ϱ_* is the characteristic mass density, T_* is the characteristic temperature, $V_* = \sqrt{\gamma T_*/m_i}$ is the characteristic sound speed, and $\nu_* = 8\pi(\varrho_*/m_i)e^4 \ln\Lambda/m_e^2 v_b^3$ is the characteristic collision frequency.

We consider a solution of the fluid equations that assumes mass density is a Gaussian along the field line that varies in time, the wake expands linearly, and temperature is constant along the field line (due to constant heating):

$$\varrho(L,t) = \sqrt{k(t)}\exp\left(-k(t)L^2\right), \tag{36}$$

$$V(L,t) = \Omega(t)L, \tag{37}$$

$$T(L,t) = T(t). \tag{38}$$

Equations 30, 33 and 34 reduce to the three ordinary differential equations for the functions of time $k(t)$, $\Omega(t)$, and $T(t)$:

$$\frac{\mathrm{dk}}{\mathrm{dt}} + 2k\Omega = 0, \tag{39}$$

$$\frac{\mathrm{d}\Omega}{\mathrm{dt}} + \Omega^2 - 2kT = 0, \tag{40}$$

$$\frac{1}{\gamma - 1}\frac{\mathrm{dT}}{\mathrm{dt}} + \Omega T = \frac{T_b}{T_*}A. \tag{41}$$

Unknown functions $k(t)$, $\Omega(t)$, and $T(t)$ are determined numerically, and the background density and temperature are treated as constants.

5.3. Modelling the wake expansion in JET plasmas

Equations 28, 29, and 35 to 41 are applied to model the wake density, $n_w(r,\theta,\zeta) = \varrho/m_i$, due to a pellet injected on the inboard track of JET.

The radial density profile (displayed in Figure 11) approximates the D_α emission profile [16], and the electron density profile measured by LIDAR 20 ms after pellet injection. The poloidal profile of the wake is initialised with a Gaussian that peaks at $\theta_0 = 5\pi/4$ with width $\Delta\theta = \pi/8$. The toroidal profile of the wake is initialised as a highly peaked Gaussian with length 4 cm. The shape in the poloidal and toroidal directions at later times is determined by the model. The 1D expansion of the wake is then mapped onto the magnetic field line that corresponds to the local q value.

The wake expands from the high field side of the tokamak, and the diffuse tail expands around the tokamak to the low field side in both directions, as demonstrated in Figure 12. The corresponding ion density of a prolate spheroid (cigar-shaped) wake of length 4 cm [28] is $n_* = 6.8 \times 10^{22}$ m^{-3}, although this is not resolved in our simulation due to the limited 3D equilibrium grid size.

The diffuse tail of the wake extends around the circumference of the tokamak, $2\pi R_0$, within ~ 1 ms. However, a large proportion of the wake remains

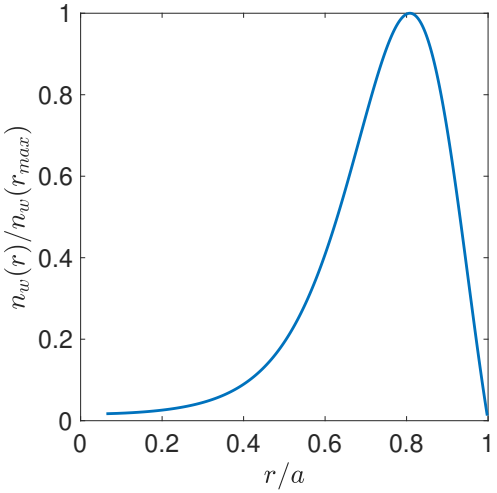

Figure 11: The radial ion density profile of the pellet wake $n_w(r)$, where the density is normalised to the maximum value at $r_{max} \approx 0.84$.

localised at the initial position. Both the poloidal and toroidal profiles are still highly inhomogeneous. The flux surface is filled in with pellet material as the tail of the wake expands along the field line.

Equation 20 suggests the width of the inner layer – where coupling dominates – is $\Delta_m^{in} \simeq 0.05$ for a TAE with toroidal mode number $n = 6$. This is much smaller than the radial width of the pellet ~ 0.2. Therefore Alfvén eigenmodes can be used to diagnose the local density at the mode location.

6. Modelling Alfvén eigenmodes in pellet injected plasmas in JET

The pellet material expands slowly compared to the Alfvénic time, therefore the non-uniform ion density profile can be treated as static. AE3D is run for a set of 3D density profiles to see how the Alfvén eigenfrequencies evolve with the expansion of the pellet wake. We use a Jacobi-Davidson QZ (JDQZ) algorithm [14] to calculate the Alfvén eigenmodes and the associated eigenfrequencies. This method significantly reduces the computational workload by only calculating a set of 40 eigenmodes that are clustered around a target frequency.

6.1. TAE frequency sweeping

The frequency evolution of a TAE as the pellet wake expands can be split into three stages: (1) the eigenfrequency increases slightly by $\sim$ kHz over a time scale of $\sim$ ms, (2) the eigenfrequency drops dramatically by $\sim$ 60 kHz over $\sim$ 10 ms, and (3)

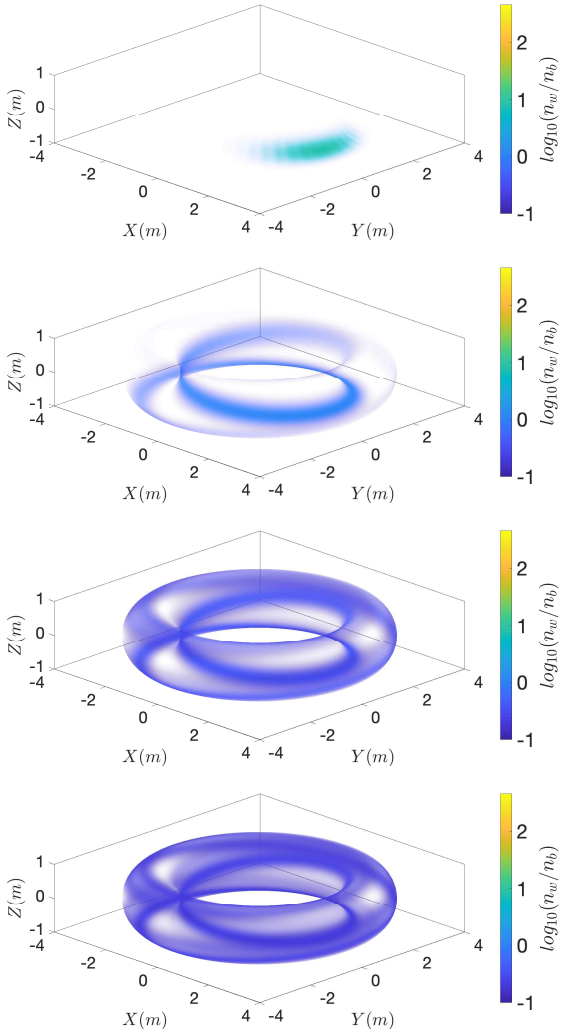

Figure 12: The 3D ion density profile of the pellet wake at times (a) $t = 0.66$ ms, (b) $t = 5.30$ ms, (c) $t = 14.58$ ms, and (d) $t = 25.85$ ms after ablation. Colour shows $\log_{10}(n_w/n_b)$, where n_w is the wake density and $n_b = 10^{19}$ m^{-3} is the equilibrium density, at the position of the maxima of the radial density profile. The initial density for a cigar-shaped wake of length 4 cm would be $n_* = 6.8 \times 10^{22}$ m^{-3}. The pellet material expands along the $q = 3.35$ field line in a plasma with background temperature $T_b = 1$ keV.

the frequency sweeping slows and the eigenfrequency stabilises. Henceforth, we define the time (t) from the beginning of the simulation, after the ablation and ionisation of the pellet material.

Initially the frequency of the $n = 6$ TAE under consideration, $f_1 = 224$ kHz, as shown in Figure 13. For the first 2 ms, the TAE eigenfrequency slightly increases (stage 1) as the wake expands from the initial poloidal position $\theta_0 = 5\pi/4$. This increase in frequency is caused by the expansion of the wake to $\theta \approx \pi$, where

the poloidal inhomogeneity in ion density produces the greatest increase in frequency. As the expansion proceeds and the wake expands to the low field side at time $t = 2.0$ ms, the TAE eigenfrequency begins to rapidly decrease (stage 2). The rate of frequency sweeping peaks at $t = 6.6$ ms. The TAE eigenfrequency stabilises as the wake homogenises in poloidal angle (stage 3). By $t = 19.2$ ms, the TAE frequency is stable at $f_2 = 156$ kHz.

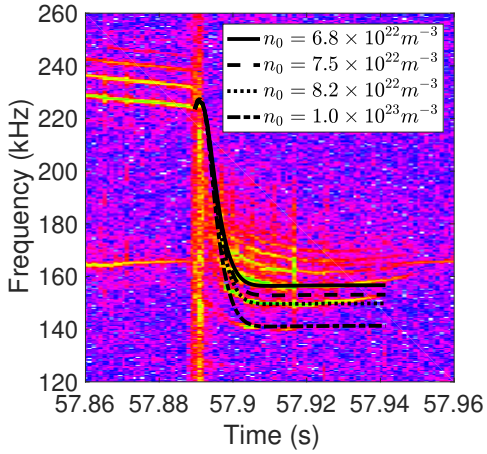

Figure 13: As the wake expands around the tokamak, the frequency of the $n = 6$ TAE drops. Numerical estimates of the TAE eigenfrequency (black) are overlaid on the experimental magnetic spectrograph for shot #49044. The eigenfrequency is calculated for four estimates of the initial ion density n_*.

The frequency sweeping ends when the ion density is homogeneous in poloidal angle. Figure 14 shows the wake density averaged over toroidal angle ζ, $\langle n_w \rangle_\zeta$. Although still highly inhomogeneous in toroidal angle (as seen in Figure 12), the ion density is poloidally homogeneous to within 10% by $t = 14.6$ ms. The rate of change of the TAE frequency at $t = 14.6$ ms is ~ 16 times slower than the maximum rate of frequency sweeping at $t = 6.6$ ms.

The magnitude of the frequency drop depends on the initial ion density of the pellet wake. Therefore, the experimental initial wake density can be estimated by matching the experimental TAE frequency drop after pellet injection with the numerical estimate. Using this new form of MHD spectroscopy, we estimate the initial pellet wake density, for cigar-shaped wake of length 4cm, to be $n_* = 6.8 \times 10^{22}$ m^{-3} for shot #49044 for the pellet injected at time $t = 17.889$ s.

6.2. Effect of q on TAE frequency sweeping

The reconstruction of the safety factor (q) profile is not accurate due to the lack of constraints on the solution

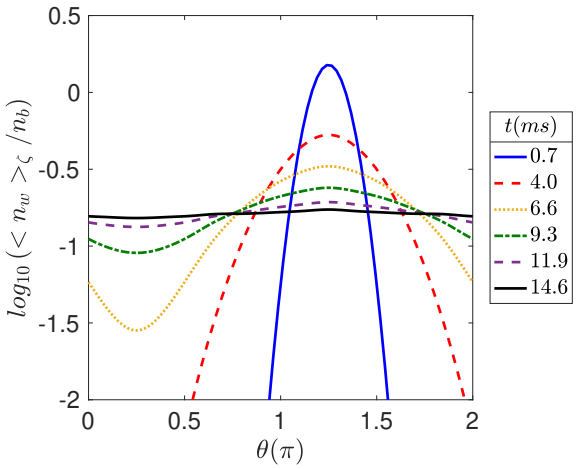

Figure 14: The logarithm of the wake density averaged over toroidal angle ζ normalised to the background density n_b, $\log_{10}(\langle n_w \rangle_\zeta / n_b)$, as a function of poloidal angle, θ.

generated by EFIT. This is expected to be the largest source of error in the estimation of the initial wake density. Therefore, q is varied numerically to study the effect on the TAE frequency sweeping.

As q decreases, the fractional change in the TAE frequency increases. The fractional frequency change also increases with the initial wake density, n_*. The effect of the inaccurate q profile on the inferred value of n_* can be estimated by varying both q and n_*, and matching the numerical frequency sweeping to the experiment. Figure 15 shows that a lower value of q at the TAE location will result in a higher inferred value for the initial wake density.

The frequency initially increases by $\sim$ kHz as the wake expands further to the inboard side of the tokamak, before decreasing dramatically. This initial frequency increase becomes less prominent for lower q values. For $q \lesssim 2$, the initial increase in frequency disappears, and the TAE eigenfrequency instead drops immediately. The initial increase in frequency shown in the numerical results of Figure 13 is not seen for TAEs in the experiment, which suggests $q \lesssim 2$ at the location of the TAE.

6.3. Poloidal homogenisation of ion density

In Section 3, the size of poloidal inhomogeneity, δ, was used to derive analytical estimates for the TAE eigenfrequency. The size of poloidal inhomogeneity can be estimated by fitting the toroidal angle averaged wake density profile, $\langle n_w \rangle_\zeta$, to $\delta \cos\theta$. The pellet is injected from the high field side, with the initial poloidal profile highly peaked around $\theta_0 = 5\pi/4$.

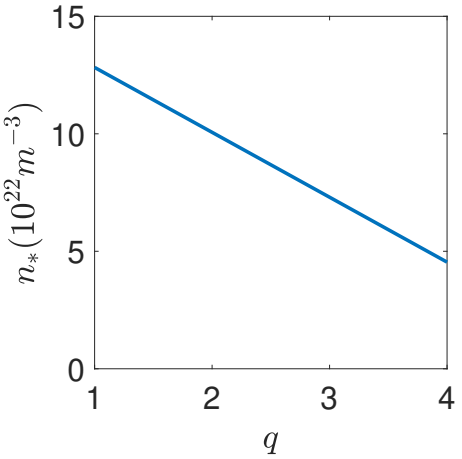

Figure 15: The inferred value of the initial wake density n_* as a function of the safety factor q at the TAE location for shot #49044.

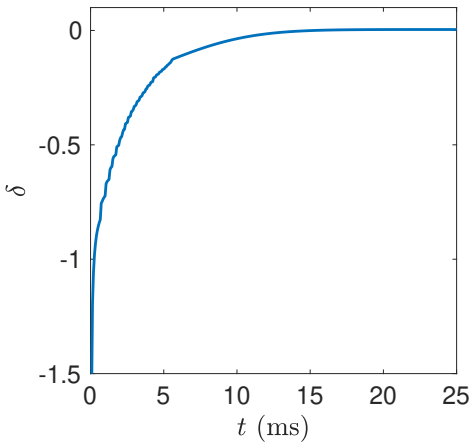

Figure 16: The size of poloidal inhomogeneity, δ, is initially a large negative number due to the initial position of the wake on the high field side. $\delta \to 0$ as the wake expands with time, t.

Therefore, δ is initially a large negative number, as shown in Figure 16. As the wake expands and the ion density homogenises, $\delta \to 0$.

Experimentally, the rapid increase in the flux surface average of the ion density as the pellet ablates occurs within $\tau \sim$ ms. The resultant decrease in the TAE eigenfrequency, $f(t) \propto v_A(t) \propto B_0/\sqrt{n_i(t)}$, would occur on the same timescale. This rapid drop in frequency is balanced by the large increase in frequency due to the density inhomogeneity coupling term $\propto \delta(t)$. As $\delta(t) \to 0$, the coupling term also decreases to zero. Therefore, the drop in frequency due to the flux surface average of the ion density is slowed from a timescale of $\tau \sim$ ms to $\tau \approx 15$ ms.

The TAE eigenfrequency $f(t)$ can be estimated from the analytical expression given by Equation 25 and the estimate of the size of poloidal inhomogeneity shown in Figure 16. The analytical estimate matches the numerical result from AE3D well for $t > 5$ ms, as demonstrated by Figure 17. For $t < 5$ ms, $|\delta|$ is large and the linear expression for the eigenfrequency is insufficient.

We can define a time in the TAE frequency sweeping at which the ion density can be said to be homogeneous, τ_h. We define this as the time at which the ratio of the maximum and minimum in the toroidal angle averaged wake density ($\langle n_w \rangle_\zeta$) is equal to 1.1. At this time there is no more than 10% variation in density with poloidal angle. This degree of inhomogeneity corresponds to $\delta \approx 0.04$.

A relationship between the experimental TAE frequency and the poloidal homogenisation time can be found from the expression for the analytical eigenfrequency (Equation 25). For an even TAE at

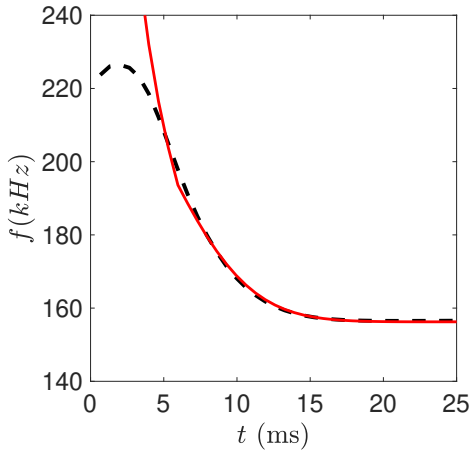

Figure 17: The TAE eigenfrequency, f, decreases with time, t. The analytical estimate of the frequency (solid red) agrees well with the numerical estimate from AE3D (dashed black) for $t > 5$ ms. For $t < 5$ ms, δ is large and the linear analytical estimate breaks down.

$r_m/a \approx 0.75$:

$$\frac{f_{TAE}(t) - f_{TAE}(t \to \infty)}{f_{TAE}(t \to \infty)} = -\frac{\delta/4}{1 - \varepsilon/2} \approx -\frac{\delta}{4}. \quad (42)$$

For $\delta(\tau_h) \approx 0.04$:

$$f_{TAE}(\tau_h) \approx 1.01 f_{TAE}(t \to \infty). \quad (43)$$

Equation 43 can be used to obtain an estimate for τ_h from the experimental TAE eigenfrequency. The time for homogenisation calculated from the

experimental TAE frequency, $\tau_h \approx 14.56 \pm 1.03$ ms, for shot #49044. This is close to the time for homogenisation calculated numerically (Figure 13 and 17), $\tau_h \approx 14.58 \pm 0.66$ ms.

6.4. Frequency sweeping of EAEs

The frequency of elliptical Alfvén eigenmodes (EAEs) also sweep in response to the expansion of the pellet wake, as demonstrated by Figure 18. The frequency drop of the EAE is reproduced for an initial ion density $n_* = 4.8 \times 10^{22}$ m^{-3} (for a 4 cm cigar-shaped wake). The initial wake density at the EAE location ($r/a \approx 0.90$) is 30% lower than the initial wake density at the TAE location ($r/a \approx 0.75$). The background temperature is lower at the EAE location, so less material ablates from the pellet than at the TAE location.

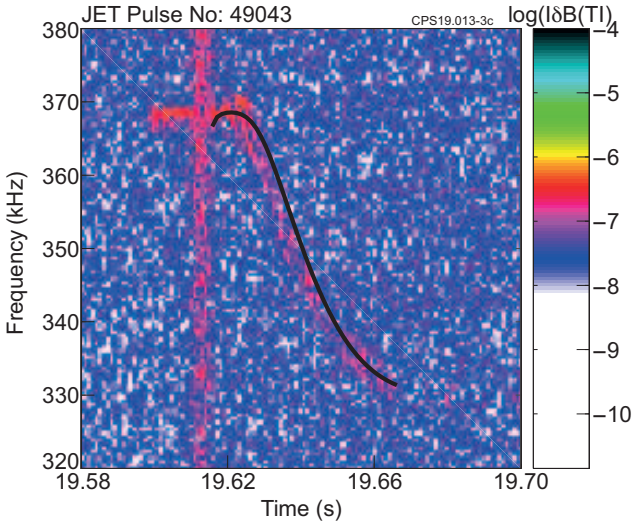

Figure 18: The EAE frequency drops as the wake expands along the $q = 5.35$ magnetic field line. The numerical reconstruction of the EAE frequency sweeping (black) is overlaid on the experimental magnetic spectrograph for shot #49043. The frequency drop matches for an initial ion density $n_* = 4.8 \times 10^{22}$ m^{-3} (for a 4 cm cigar-shaped wake).

The time evolution of the EAE frequency follows a similar pattern to that of the TAE frequency (described in Section 6.1). The frequency sweeping of the EAE also ends when the wake density homogenises poloidally. However, poloidal homogenisation is slower at the EAE location ($r/a \approx 0.90$). q at the EAE location is higher than for TAEs. Homogenisation of the wake density in the poloidal direction is slower at higher q values. Additionally, the lower background temperature near the edge also results in a slower expansion velocity. As a result, the frequency sweeping of EAEs occurs over $\tau_h \approx 50$ ms, 2.7 longer than for TAEs.

The initial increase in frequency (stage 1 of the frequency sweeping) occurs over a longer period for higher q values due to the slower expansion to the low field side. Therefore, there is a longer delay before the drop in EAE frequency. There is a delay of 9.3 ms before frequency sweeping begins for $q = 5.35$. This qualitatively matches the experimental observation of a delay in EAE frequency sweeping after pellet injection. However, the experimentally observed delay was longer, averaging 12.8 ms. The difference between the numerical and experimental result may be due to lower background plasma temperature at the EAE position compared to the TAE position. This decreases the rate of power transfer from the background electrons to the wake electrons, resulting in a lower wake temperature and slower expansion.

7. Discussion

Only the 1D expansion of the wake along the field line is included in this study. The cross-field movement of the wake due to the $E \times B$ force is not considered. Additionally, cross-field diffusion is not included and may be important at late times. The frequency sweeping is still well reproduced despite these limitations.

The timescale for frequency sweeping and the fractional change in frequency for TAEs and EAEs were compared for inboard and outboard pellet injection in Table 1. As shown in the previous section, these timescales are related to the time required for poloidal homogenisation of the ion density profile. This suggests the average time required for poloidal homogenisation of the ion density at the TAE location is 18 ms for inboard pellet injection.

This relationship suggests that the ion density profile produced by outboard pellet injection takes 1.4 times longer to homogenise poloidally than for inboard pellet injection, at the location of both TAEs and EAEs. The pellet density at the EAE location ($r/a \approx 0.9$) takes 2.7 times longer to homogenise poloidally than the material at the TAE location ($r/a \approx 0.75$), for both inboard and outboard pellet injection. This is likely to be due to the higher q at higher radii. Consequently, shallow pellets — which will expand along higher q field lines — could take longer to homogenise poloidally.

The fractional change in eigenfrequency depends on the initial ion density of the wake at the mode location. The relative fuelling efficiency of inboard and outboard pellet injection can be calculated by matching the numerical fractional frequency change to the experimental values for inboard and outboard

pellet injection. Inboard fuelling deposits more 4 times more material than outboard fuelling at the TAE location. The discrepancy in fuelling efficiency with the injection track [6] is caused by the ∇B-induced drift of the deposited plasmoid, which causes an acceleration to the outboard side. As a result, material injected on the outboard track is more easily ejected from the plasma compared to material injected on the inboard track.

EAEs do not show the discrepancy in fuelling efficiency between inboard and outboard injection. This suggests the change in ion density due to a pellet at the plasma edge is similar for inboard and outboard injection. Additionally, the fuelling efficiency for outboard injection is equally poor at the location of the TAEs and EAEs. Conversely, only the fuelling efficiency in the core is improved for inboard injection.

The experimental fractional change in TAE frequency for shot #49044 was replicated by a simulation with an initial ion density for a 4cm cigar-shaped ablatant $n_* = 6.8{\times}10^{22}$ m^{-3}. This value agrees well with experimental observations made on different machines, $n_* \sim 10^{23}$ m^{-3} [30, 31, 32, 33]. The value found here is slightly lower because the TAEs under consideration were not located at the peak of the radial ablation profile ($r/a \approx 0.84$). Additionally, a more accurate reconstruction of the q profile may increase the inferred value of the initial ion density.

Previous simulations have suggested the plasma returns to a steady state after 28 ms [7]. This is longer than the poloidal homogenisation time found in this study, $\tau_h \approx 15$ ms, but includes radial transport of the pellet material.

During the experiment, there is a short period $\sim 3{-}8$ ms where the toroidal mode numbers of the Alfvén eigenmodes can not be determined. The time scale of this period is consistent with the time taken for the pellet to travel through the plasma. For inboard (HFS) injection, most of the pellet material was deposited in the first 1.15m of the track, which suggests the time of flight of the pellet was $\tau_{ToF} \gtrsim 1.15/v_{pell} \approx 7$ ms. Magnetic reconnection will occur as the pellet ablates and ionises [34]. The broadband magnetic perturbation seen on the spectrograph during this period may be a signal of this magnetic reconnection. The effect of the wake on the equilibrium is not considered here, and therefore the effect of magnetic reconnection is outside the scope of our study.

8. Summary

To use Alfvén eigenmodes for MHD spectroscopy of plasmas fuelled with pellet injection, the 3D MHD codes Stellgap and AE3D were generalised to incorporate 3D density profiles. A model for the 1D expansion of the ionised pellet wake along a magnetic field line was derived from the fluid equations. This model of the wake expansion provided a 3D density profile as input for AE3D. Thereby, the time evolution of the Alfvén eigenfrequency was reproduced.

By comparing the numerical frequency drop to that of the experiment, the initial ion density of a cigar-shaped ablation region of length 4cm is estimated to be $n_* = 6.8 \times 10^{22}$ m^{-3} at the TAE location ($r/a \approx 0.75$). This value is in good agreement with previously measured values. By reproducing the frequency evolution of the elliptical Alfvén eigenmode (EAE), the initial ion density at the EAE location ($r/a \approx 0.9$) is estimated to be $n_* = 4.8 \times 10^{22}$ m^{-3}.

The frequency sweeping of the Alfvén eigenfrequency ends when the ion density homogenises in poloidal angle. Therefore, the time for poloidal homogenisation of the ion density after pellet ablation is $\tau_h \approx 15$ ms for the analysed discharge. We can determine the experimental homogenisation time τ_h from the TAE frequency evolution using our analytical expression. For poloidal homogenisation of the wake density to within 10%, $f(\tau_h) = 1.01 f(t_2)$, where $f(t_2)$ is the frequency at the end of the frequency sweeping.

This modelling suggests that the time for poloidal homogenisation of the ion density at the TAE position is $\tau_h = 18 \pm 4$ ms for inboard pellet injection, and $\tau_h = 26 \pm 2$ ms for outboard pellet injection. Poloidal homogenisation of the ion density takes 2.7 times longer at the EAE location than at the TAE location for both inboard and outboard pellet injection.

Acknowledgments

This paper benefited from comments by D Keeling and J Mailloux. This work has been carried out within the framework of the EUROfusion Consortium and has received funding from the Euratom research and training programme 2014-2018 and 2019-2020 under grant agreement No 633053 and from the RCUK Energy Programme [grant number EP/P012450/1]. The views and opinions expressed herein do not necessarily reflect those of the European Commission. This research was also supported by the U.S. Department of Energy under Grant No. DE-FG02-04ER54742 (IFS).

References

[1] K. L. Wong. A review of Alfvén eigenmode observations in toroidal plasmas. *Plasma Physics and Controlled Fusion*, 41(1):R1, 1999.

[2] C. Z. Cheng, Liu Chen, and M. S. Chance. High-n ideal and resistive shear Alfvén waves in tokamaks. *Annals of Physics*, 161(1):21 – 47, 1985.

[3] R. L. Dewar, R. C. Grimm, J. L. Johnson, E. A. Frieman, J. M. Greene, and P. H. Rutherford. Long-wavelength

kink instabilities in lowpressure, uniform axial current, cylindrical plasmas with elliptic cross sections. *Physics of Fluids*, 17(5):930–938, 1974.

[4] R. Betti and J. P. Freidberg. Ellipticity induced Alfvén eigenmodes. *Physics of Fluids B: Plasma Physics*, 3(8):1865–1870, 1991.

[5] N. Nakajima, C. Z. Cheng, and M. Okamoto. High-n helicity-induced shear Alfvén eigenmodes. *Physics of Fluids B: Plasma Physics*, 4(5):1115–1121, 1992.

[6] P. T. Lang, K. Büchl, M. Kaufmann, R. S. Lang, V. Mertens, H. W. Müller, and J. Neuhauser. High-Efficiency Plasma Refuelling by Pellet Injection from the Magnetic High-Field Side into ASDEX Upgrade. *Phys. Rev. Lett.*, 79:1487–1490, Aug 1997.

[7] L. Garzotti, X. Garbet, A. Thyagaraja, M. R. de Baar, D. Frigione, P. Mantica, V. Parail, B. Pégourié, L. Zabeo, and JET EFDA contributors. Simulations of JET pellet fuelled ITB plasmas. *Nuclear Fusion*, 46(1):73, 2006.

[8] P. T. Lang, B. Alper, R. Buttery, K. Gal, J. Hobirk, J. Neuhauser, M. Stamp, and JET-EFDA contributors. ELM triggering by local pellet perturbations in type-I ELMy H-mode plasma at JET. *Nuclear Fusion*, 47(8):754, 2007.

[9] J. P. Goedbloed, H. A. Holties, S. Poedts, G. T. A. Huysmans, and W. Kerner. MHD spectroscopy: free boundary modes (ELMs) and external excitation of TAE modes. *Plasma Physics and Controlled Fusion*, 35(SB):B277, 1993.

[10] S. E. Sharapov, H. J. C. Oliver, B. N. Breizman, M. Fitzgerald, L. Garzotti, and JET contributors. MHD spectroscopy of JET plasmas with pellets via Alfvén eigenmodes. *Nuclear Fusion*, 58(8):082008, 2018.

[11] S. E. Sharapov, B. Alper, H. L. Berk, D. N. Borba, B. N. Breizman, C. D. Challis, A. Fasoli, N. C. Hawkes, T. C. Hender, J. Mailloux, S. D. Pinches, and D. Testa. Alfvén wave cascades in a tokamak. *Physics of Plasmas*, 9(5):2027–2036, 2002.

[12] A. Fasoli, D. Testa, S. Sharapov, H. L. Berk, B. Breizman, A. Gondhalekar, R. F. Heeter, M. Mantsinen, and contributors to the EFDA-JET Workprogramme. MHD spectroscopy. *Plasma Physics and Controlled Fusion*, 44(12B):B159, 2002.

[13] D. A. Spong, R. Sanchez, and A. Weller. Shear Alfvén continua in stellarators. *Physics of Plasmas*, 10(8):3217–3224, 2003.

[14] D. A. Spong, E. D'Azevedo, and Y. Todo. Clustered frequency analysis of shear Alfvén modes in stellarators. *Physics of Plasmas*, 17(2):022106, 2010.

[15] P. H. Rebut, R. J. Bickerton, and B. E. Keen. The Joint European Torus: installation, first results and prospects. *Nuclear Fusion*, 25(9):1011, 1985.

[16] T. T. C. Jones, L. R. Baylor, C. D. Challis, S. J. Cox, C. Gormezano, C. W. Gowers, L. D. Horton, P. T. Lang, P. J. Lomas, G. F. Matthews, G. Saibene, P. Twynam, A. D. Walden, M. J. Watson, S. Wijetunge, and B. L. Willis. Results of JET Pellet Fuelling Experiments with Outboard and Inboard Launch. In *Proceedings of 27th EPS Conference on Controlled Fusion and Plasma Physics Budapest, 12-16 June 2000*, volume 24B of *ECA*, pages 13–16, 2000.

[17] H. Salzmann, J. Bundgaard, A. Gadd, C. Gowers, K. B. Hansen, K. Hirsch, P. Nielsen, K. Reed, C. Schrödter, and K. Weisberg. The LIDAR Thomson scattering diagnostic on JET (invited). *Review of Scientific Instruments*, 59(8):1451–1456, 1988.

[18] R. F. Heeter, A. F. Fasoli, and S. E. Sharapov. Chaotic Regime of Alfvén Eigenmode Wave-Particle Interaction. *Phys. Rev. Lett.*, 85:3177–3180, Oct 2000.

[19] H. L. Berk, J. W. Van Dam, Z. Guo, and D. M. Lindberg. Continuum damping of low-n toroidicity-induced shear Alfvén eigenmodes. *Physics of Fluids B: Plasma Physics*, 4(7):1806–1835, 1992.

[20] Ya. I. Kolesnichenko, V. V. Lutsenko, H. Wobig, Yu. V. Yakovenko, and O. P. Fesenyuk. Alfvén continuum and high-frequency eigenmodes in optimized stellarators. *Physics of Plasmas*, 8(2):491–509, 2001.

[21] J. Candy and M. N. Rosenbluth. Nonideal theory of toroidal Alfvén eigenmodes. *Physics of Plasmas*, 1(2):356–372, 1994.

[22] G. Y. Fu and J. W. Van Dam. Excitation of the toroidicity-induced shear Alfvén eigenmode by fusion alpha particles in an ignited tokamak. *Physics of Fluids B: Plasma Physics*, 1(10):1949–1952, 1989.

[23] B. N. Breizman and S. E. Sharapov. Energetic particle drive for toroidicity-induced Alfvén eigenmodes and kinetic toroidicity-induced Alfvén eigenmodes in a low-shear tokamak. *Plasma Physics and Controlled Fusion*, 37(10):1057, 1995.

[24] A. B. Mikhailovskii. *Instabilities in a Confined Plasma (Series in Plasma Physics)*. IOP Publishing Ltd, 1st edition, 1998.

[25] M. Abramowitz and I. A. Stegun, editors. *Handbook of Mathematical Functions with Formulas, Graphs, and Mathematical Tables*. Dover Publications, 10th edition, 1972.

[26] S. P. Hirshman and J. C. Whitson. Steepest-descent moment method for three-dimensional magnetohydrodynamic equilibria. *The Physics of Fluids*, 26(12):3553–3568, 1983.

[27] L. L. Lao, H. St. John, R. D. Stambaugh, A. G. Kellman, and W. Pfeiffer. Reconstruction of current profile parameters and plasma shapes in tokamaks. *Nuclear Fusion*, 25(11):1611, 1985.

[28] B. Pégourié. Review: Pellet injection experiments and modelling. *Plasma Physics and Controlled Fusion*, 49(8):R87, 2007.

[29] B. A. Trubnikov. Particle Interactions in a Fully Ionized Plasma. *Reviews of Plasma Physics*, 1:105, 1965.

[30] TFR group. Pellet injection experiments on the TFR tokamak. *Nuclear Fusion*, 27(12):1975–1999, dec 1987.

[31] R. D. Durst, W. L. Rowan, M. E. Austin, R. A. Collins, R. F. Gandy, P. E. Phillips, and B. Richards. Experimental observations of the dynamics of pellet ablation on the Texas Experimental Tokamak (TEXT). *Nuclear Fusion*, 30(1):3–9, jan 1990.

[32] H. Sakakita, K. N. Sato, I. Nomura, Y. Hamada, A. Nishizawa, Y. Kawasumi, K. Ida, J. Xu, K. Narihara, K. Toi, A. Ejiri, T. Seki, K. Adachi, H. Iguchi, A. Fujisawa, R. Liang, M. Sakamoto, Y. Kano, S. Hirokura, S. Hidekuma, and M. Kojima. Measurement of ablation cloud parameters and plasma potential with on/off-axis pellet injection in the JIPP T-IIU tokamak. *Fusion Engineering and Design*, 34-35:329 – 332, 1997. Fusion Plasma Diagnostics.

[33] H. W. Müller, R. Dux, M. Kaufmann, P. T. Lang, A. Lorenz, M. Maraschek, V. Mertens, J. Neuhauser, and ASDEX Upgrade Team. High β plasmoid formation, drift and striations during pellet ablation in ASDEX Upgrade. *Nuclear Fusion*, 42(3):301–309, 2002.

[34] H. R. Strauss and W. Park. Magnetohydrodynamic effects on pellet injection in tokamaks. *Physics of Plasmas*, 5(7):2676–2686, 1998.